Electronic Supplementary Information

Sustainable energy harvesting via a scalable Janus photonic metamaterial for thermoelectric generation

Ningning Song,[a] Haonan Shi, [a] Hao Pan, [b,c] Xuefei Zhang, [a] Runni Zhao, [a] Junming Zhang, [a] Lian Zuo,[d] Xiaonan Deng, [a,d,e] Meng Song, [a,d,e] Zeli Wang, [a,d,e] Jinghui Huang, [f] Chen Wang, [a,d,e] Peiyao Zhao, [a] Xiaohui Wang, [a] Wei Li, [b,c] Guangming Tao, [g,h] Yongzheng Wen , [a] Jingbo Sun, [a] Ji Zhou *[a]

[a] *State Key Laboratory of New Ceramic Materials, School of Materials Science and Engineering, Tsinghua University, Beijing 100084, China*

[b] *GPL Photonics Laboratory, State Key Laboratory of Luminescence Science and Technology, Changchun Institute of Optics, Fine Mechanics and Physics, Chinese Academy of Sciences, Changchun, Jilin, 130033, P. R. China*

[c] *University of Chinese Academy of Sciences, Beijing, 100049, China*

[d] *Key Laboratory of Advanced Materials (MOE), School of Materials Science and Engineering, Tsinghua University, Beijing 10084, China*

[e] *Beijing Advanced Innovation Center for Integrated Circuits, Beijing, China, 100084*

[f] *State Key Laboratory of Information Photonics and Optical Communications, School of Physical Science and Technology, Beijing University of Posts and Telecommunications, Beijing 100876, China*

[g] *Research Center for Intelligent Fiber Devices and Equipment, Wuhan National Laboratory for Optoelectronics, Huazhong University of Science and Technology, Wuhan 430074, China*

[h] *Center for Intelligent Health Interdisciplinary Science, Central China Normal University, Wuhan 430079, China.*

* Corresponding author. E-mail address: zhouji@tsinghua.edu.cn

Supporting Discussions

Note S1. Numerical Simulation of Optical Properties.

The scattering characteristics of particles with specific geometries (e.g., spheres and flakes) were computationally investigated utilizing the Finite Element Method (COMSOL Multiphysics 6.3) and the Discrete Dipole Approximation (DDSCAT 7.3). The refractive indices of the polymer matrix and the h-BNNs were defined as 1.45 and 2.0, respectively. For the COMSOL simulations, planar flakes were modeled with radius ranging from 0.1 to 0.5 μm and a fixed thickness of 40 nm. The target particle was embedded in a polymer medium, and the entire computational domain was enclosed by perfectly matched layers (PMLs) with matched optical properties. These PMLs effectively absorb outgoing scattered waves, allowing the scattering efficiency to be accurately derived from the calculated scattering cross-section. Furthermore, a specific flake with a 0.3 μm radius was selected to analyze the angular dependence of scattering. Under an incident electromagnetic wavelength of 0.7 μm, the scattering efficiency was calculated at varying angles of incidence using both COMSOL and DDSCAT. For the periodic pyramid metastructure, the optical response was simulated using a single unit cell. PMLs and periodic ports were assigned to the top and bottom boundaries of the computational domain. The reflectance R and transmittance T were extracted directly from the port parameters, and the absorptivity and emissivity of the structure was subsequently calculated as 1-R-T.

Note S2. Calculation of the Radiative Cooling Power.

The net energy flux of the sample is determined by solar radiation, the downward atmospheric thermal radiation, and the convective and conductive heat exchange with the ambient environment. The net cooling power can be estimated from

$$P_{net} = P_r - P_a - P_{nonrad} - P_{sun} \quad \backslash* \text{ MERGEFORMAT (S1)}$$

where P_r is the radiated power of the samples, P_a is the absorbed downward atmospheric thermal radiation power, P_{nonrad} is the non-radiative heat transfer power (convection and conduction), and P_{sun} is the absorbed solar power.

The radiated power of the samples, P_r is given by:

$$P_r = 2\pi \int_0^{\pi/2} \sin\theta \cos\theta d\theta \int_0^{\infty} u(\lambda, T_r) e_r(\lambda, \theta) d\lambda \text{ * MERGEFORMAT (S2)}$$

where θ is the angle, T_r is the temperature of the sample, and $e_r(\lambda, \theta)$ is the sample emittance as a function of wavelength λ and angle θ. u(λ,T) is the blackbody spectral radiance as a function of wavelength λ and temperature T according to Planck's law,

$$\mathrm{u}(\lambda,\mathrm{T}) = \frac{2hc^2}{\lambda^5} \frac{1}{e^{\frac{hc}{\lambda k_B T}} - 1} \qquad \text{* MERGEFORMAT (S3)}$$

where c is the speed of light, h is the Planck constant, and k_B is the Boltzmann constant.

The power absorbed from the downward atmospheric radiation is given by:

$$P_a = 2\pi \int_0^{\pi/2} \sin\theta \cos\theta d\theta \int_0^{\infty} u(\lambda, T_a) e_r(\lambda, \theta) e_a(\lambda, \theta) d\lambda \text{ * MERGEFORMAT (S4)}$$

where T_a is the ambient temperature, $e_a(\lambda, \theta) = 1 - t(\lambda)^{1/\cos\theta}$ is the atmospheric emissivity, and $t(\lambda)$ is the atmospheric transmittance.

The power absorbed by the samples from solar radiation is:

$$P_{sun} = \int_0^{\infty} e_r(\lambda, \theta) I_{AM1.5}(\lambda) d\lambda \quad \text{* MERGEFORMAT (S5)}$$

where $I_{AM1.5}(\lambda)$ is the spectral irradiance of the Air Mass 1.5 solar spectrum.

$$P_{nonrad} = h_c (T_a - T_r) \qquad \text{* MERGEFORMAT (S6)}$$

where h_c is the non-radiative heat transfer coefficient between the ambient environment and the cooling object, accounting for both convection and conduction.

Note S3. Numerical Simulation of Temperature Distribution

To elucidate the temperature gradient within the architecture, numerical simulations were performed via COMSOL Multiphysics. A standard solar irradiance of 1000 W/m^2 was applied to the outward-facing surface as the external radiation source. Boundary conditions accounting

for nonradiative heat flux and diffuse surface radiation were applied to simulate realistic environmental heat exchange, with the ambient temperature maintained at 20 °C. The solar absorptance of the CNT is 94%, and its mid-infrared emissivity is 30%.

Note S4. Calculation of Thermoelectric Output Power Density.

$$P_o = I^2 R_l = (\frac{V}{R_{in} + R_l})^2 \times R_l \quad \text{* MERGEFORMAT (S7)}$$

where V and I denote the voltage and current with an applied external load resistance R_l, respectively, and R_{in} represents the internal resistance of the device. The maximum output power is achieved when the load resistance equals the internal resistance of device:

$$P_{\max} = \frac{V^2}{4R_{in}} \quad \text{* MERGEFORMAT (S8)}$$

Subsequently, the power density can be expressed as:

$$PD_{\max} = \frac{P_{\max}}{N \times S_C} \quad \text{* MERGEFORMAT (S9)}$$

where N is the total number of thermoelectric elements, and S_C represents the cross-sectional area of the individual thermoelectric elements perpendicular to the heat flow direction.

Experimental Methods

Materials. Polydimethylsiloxane (PDMS, Sylgard 184) was sourced from Dow Corning (USA). Hexagonal boron nitride nanosheets (h-BNNs) were obtained from Guangzhou Bingwen Trade Co., Ltd (China). Single-walled carbon nanotubes (CNTs) and compatible dispersing agents were procured from Jiangsu XFNANO Materials Tech Co., Ltd. (China). The silver paste was supplied by Dalian Ink Sensitivity Electronics Technology Co., Ltd. (China).

Fabrication of the Silicon Template with Inverted Micro-Pyramids. The silicon template featuring an inverted micro-pyramidal metastructure was fabricated via a combination of photolithography, dry etching and anisotropic wet etching. Initially, a bare (001)-oriented silicon wafer was spin-coated with photoresist and patterned via standard photolithography using a photomask with periodic square apertures. Next, a dry etching process was employed

on the exposed silicon regions to transfer the surface pattern and create initial shallow pits. Subsequently, the residual photoresist was completely stripped, yielding a clean, pre-patterned silicon wafer. The wafer then underwent anisotropic wet etching in a potassium hydroxide (KOH) solution. During this step, the initial pits guided the anisotropic etching process to develop the final inverted micro-pyramidal cavities with a target depth of 3.5 μm. Due to the crystallographic specificity of the KOH etch on the (001) silicon plane, a characteristic sidewall angle of 54.7° was naturally realized. Finally, the fabricated template was thoroughly cleaned.

Fabrication of the Janus photonic metamaterial (JPM). The polymer matrix was prepared by mixing the PDMS base and crosslinking agent at a weight ratio of 10:1. h-BNNs were incorporated into the PDMS precursor at volume fractions of 5%, 10%, 20%, and 30%. To ensure homogeneous dispersion, the mixtures were thoroughly blended, followed by a vacuum degassing step to eliminate entrapped air bubbles. The fabrication method was tailored to the viscosity of the composite mixtures. With the solid volume fraction kept at 20% or lower, the mixture maintained good fluidity, allowing it to be directly coated onto a glass substrate using a blade coater to precisely control the film thickness. Conversely, at a solid volume fraction of 30 vol%, the mixture exhibited a highly viscous, dough-like consistency. It was mechanically kneaded and subsequently processed into a film using a roll press (MSK-HRP-01, Hefei Kejing Electromechanical Technology Co., Ltd.), reducing the thickness step-by-step until the target dimension was achieved. To construct the Janus photonic metamaterial (JPM) featuring both high solar reflectance and high MIR emissivity, a 10 vol% precursor dispersion was first cast onto the prepared silicon template. This layer was subsequently placed in an oven at 75 °C for 20 min to achieve precuring. Next, the 30 vol% roll-pressed green film, serving as the reflective layer, was laminated onto the pre-cured precursor on the wafer. The bilayer assembly was then allowed to cure at 75 °C for 30 min. Finally, the integrated film was carefully peeled off the silicon substrate, yielding the complete photonic film with precisely replicated periodic pyramidal metastructures.

Fabrication of CNT films. An aqueous dispersion of single-walled carbon nanotubes (CNTs) was prepared by dispersing CNTs in deionized water at a concentration of 0.4 mg/mL, along with a dispersant added at an amount equivalent to 70% of the CNT mass. The suspension was then magnetically stirred for 24 hours to ensure homogeneous dispersion. The dispersion was

then vacuum filtered through a polytetrafluoroethylene (PTFE) membrane (0.1μm pore size) and dried at 60 ℃ to form the CNT film.

Fabrication of the integrated Janus photonic metamaterial-based thermoelectric device (JPM-TED). To assemble the integrated device, a bottom substrate was first prepared by blade-coating the polymer composite with a 10 vol% h-BN filler loading, then transferred to an oven for a precuring process. Subsequently, an array of macroscopic CNT films was precisely arranged atop this layer, and the individual elements were electrically connected via silver paste. Following this, the prefabricated JPM was tailored to the desired dimensions and carefully laminated to cover one end of the CNT elements. Finally, the entire stacked assembly was subjected to a complete thermal curing process, seamlessly bonding the components into a unified, monolithic device.

Characterization. The micro-morphology of the films was examined using a field-emission scanning electron microscope (FE-SEM; MERLIN Compact, Carl Zeiss AG). Solar spectral reflectance (including both specular and diffuse components) was measured using a UV-Vis-NIR spectrophotometer (Cary 5000, Agilent) equipped with an integrating sphere. Mid-infrared emissivity (E) was derived from reflectance (R) and transmittance (T) spectra acquired via a Fourier transform infrared spectrometer (FTIR; Nicolet iS50, Thermo Fisher) coupled with a gold-coated integrating sphere (PIKE Technologies), calculated based on Kirchhoff's law as $E = A - 1 - R - T$. Thermal conductivity was determined using the transient plane source (TPS) method (Hot Disk TPS 3500), in strict accordance with ISO 22007-2:2015 and GB/T 42919.1-2023 standards. Surface wettability was assessed by measuring the water contact angle via the sessile drop method using an optical contact angle meter (OCA25, DataPhysics). Temperature data were logged using K-type thermocouples connected to a data acquisition module (DAM3138, Beijing Art Technology Development Co., Ltd.). Electrical signals were recorded using a digital multimeter (Keysight 34461A, Keysight Technologies). Simulated solar irradiation was provided by a commercial solar simulator (CEL-PF300-T10, Beijing CEAULIGHT, China).

Supplementary Figures

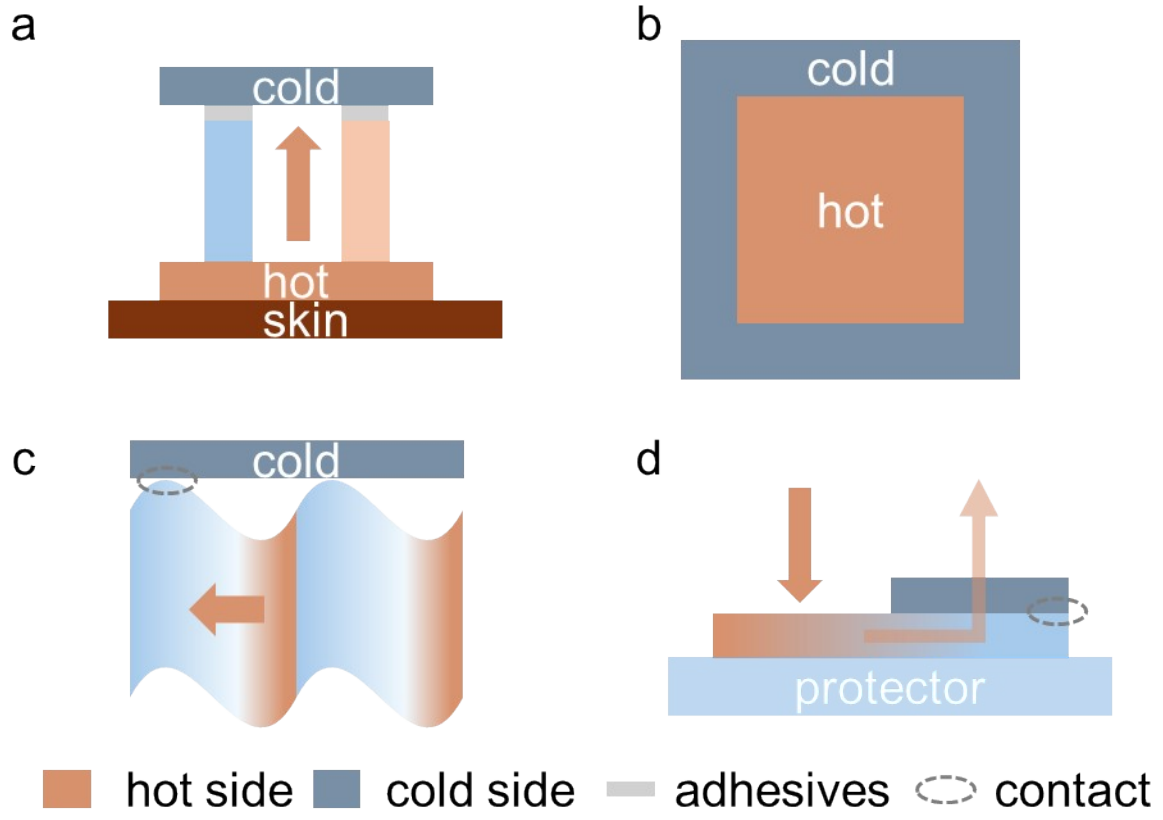

Fig. S1. Comparison of structures and thermal transport mechanisms in RC-TE systems. (a) vertical stacking with adhesive layers, introducing additional interfacial thermal resistance; downward heat accumulation, and the consequent thermal burden inflicted on the human body. (b) Rigid and bulky assemblies. (c) Irregular flexible architectures (e.g., wavy structures), suffering from restricted interfacial contact area and air voids, which disrupt the thermal continuum. (d) Our monolithic sandwich architecture, featuring seamless conformal contact that ensures continuous heat transfer and provides active thermal protection for the underlying objects.

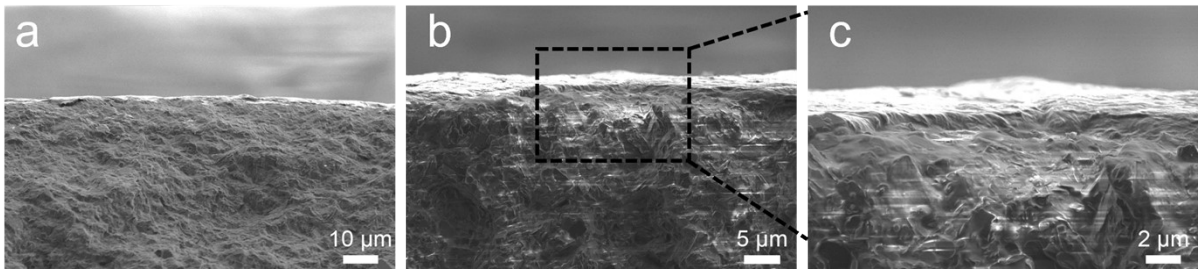

Fig. S2. Cross-sectional SEM images of the CNT-JPM junction. (a–c) Morphology of the interface viewed under different magnifications with scale bars of (a) 10μm, (b) 5μm, and (c)

2μm.

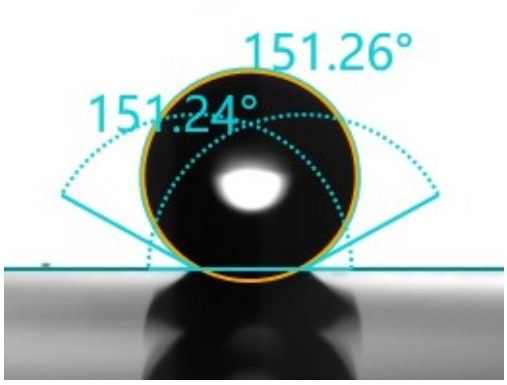

Fig. S3. Optical image of the water contact angle on the surface of the film featuring periodic pyramidal metastructures.

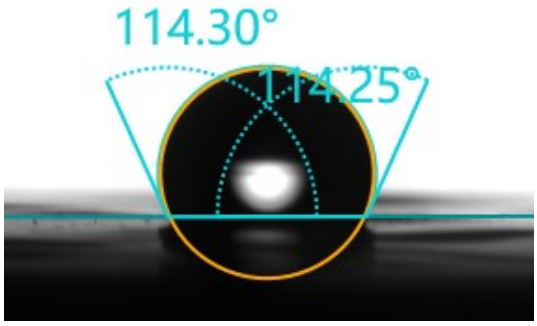

Fig. S4. Optical image of the water contact angle on the flat film.

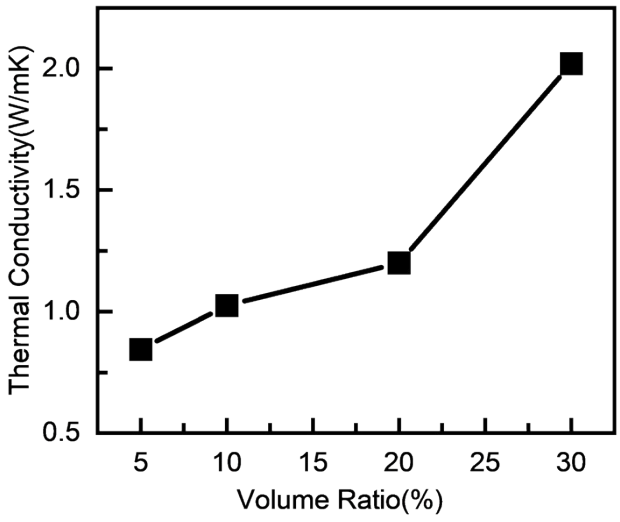

Fig. S5. Thermal conductivity of the composite films as a function of the h-BNN volume fraction.

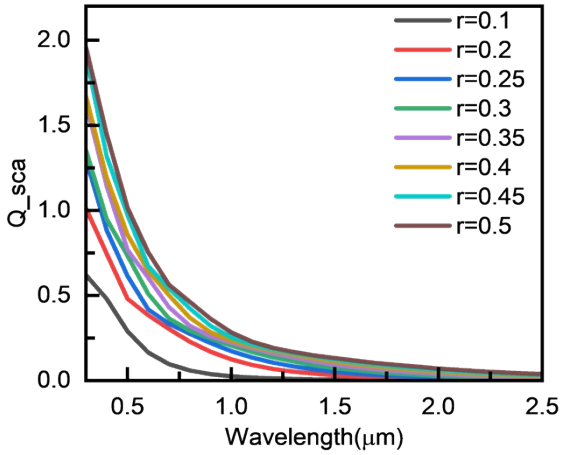

Fig. S6. Wavelength dependence of scattering efficiency for different planar flake radius.

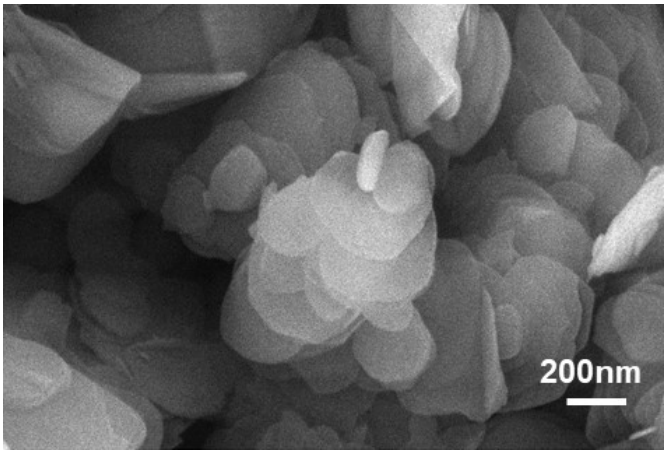

Fig. S7. SEM images of the h-BNNs.

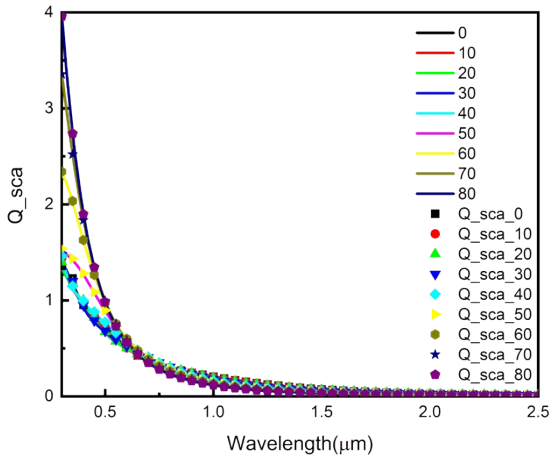

Fig. S8. Scattering efficiency of the h-BN flakes (radius = 0.3 μm) as a function of incident angle (from 0° to 80°) at a wavelength of 0.7 μm. Solid lines and symbols denote the results obtained from COMSOL simulations and DDSCAT calculations, respectively.

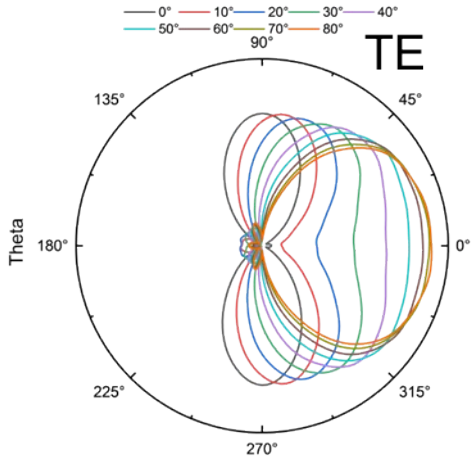

Fig. S9. 2D far-field radiation patterns of the planar flakes under TE-polarized electromagnetic wave incidence from 0° to 80°.

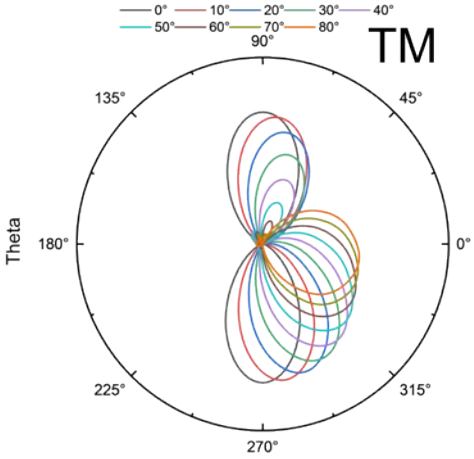

Fig. S10. 2D far-field radiation patterns of the planar flakes under TM-polarized electromagnetic wave incidence from 0° to 80°.

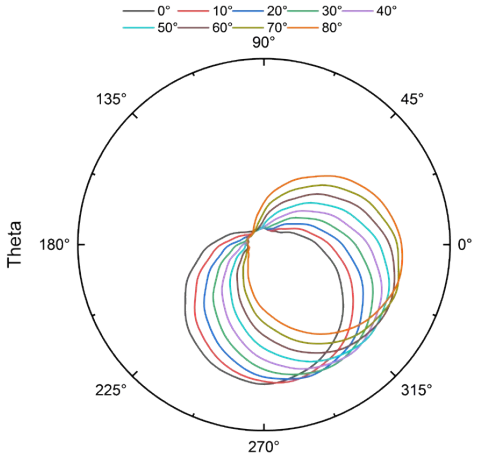

Fig. S11. 2D far-field radiation patterns of the spherical particles under electromagnetic wave incidence from 0° to 80°.

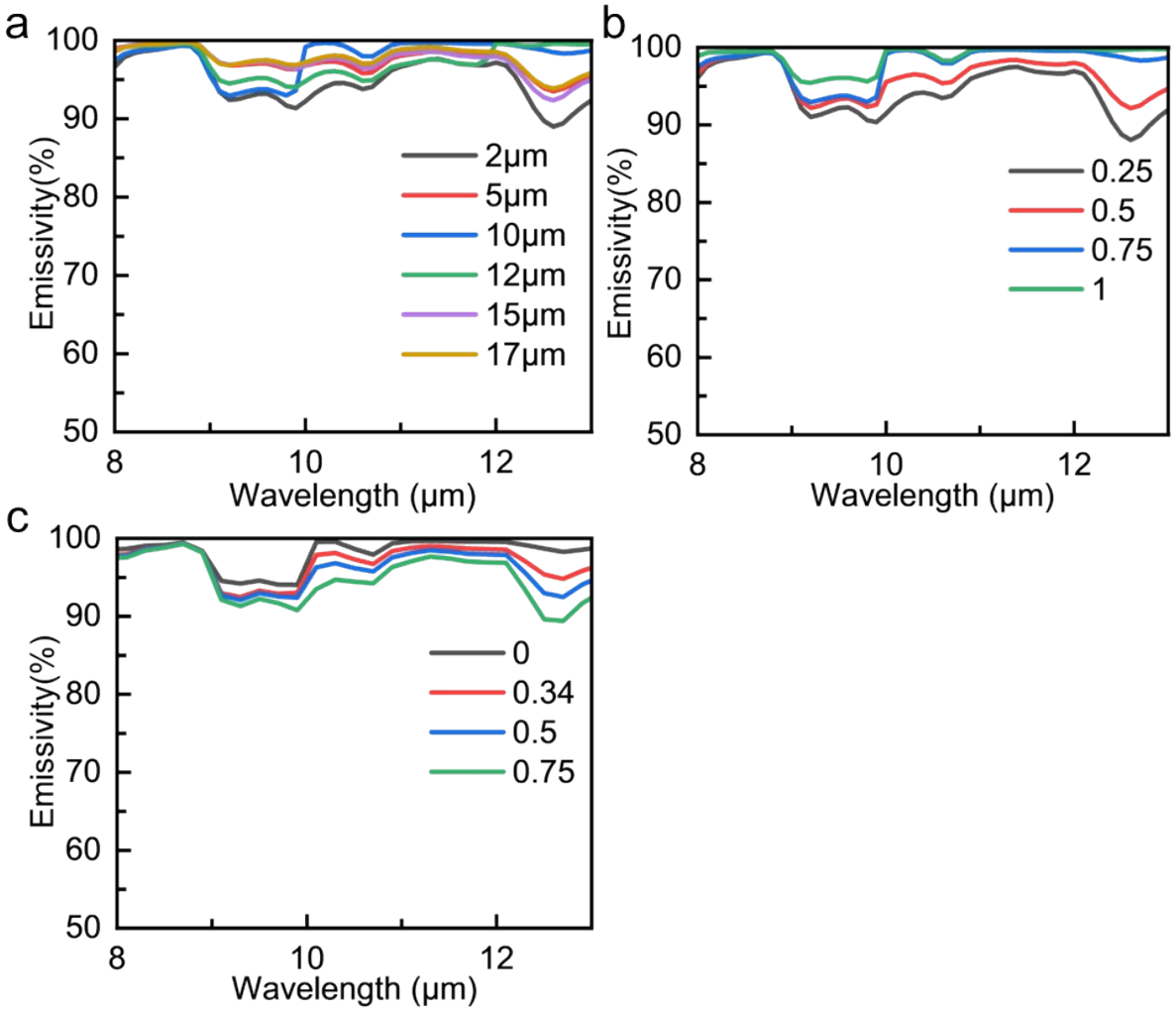

Fig. S12 Optical simulations for structural optimization. Dependence of the MIR emissivity within the atmospheric window on (a) varying periods, (b) different fill factors, and (c) top-to-base area ratios of the pyramidal arrays.

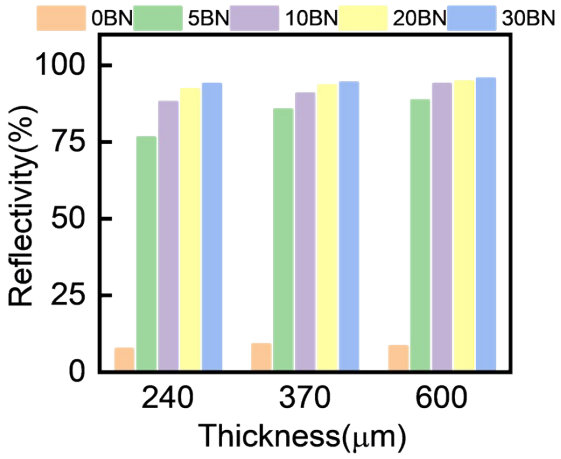

Fig. S13. Solar reflectance of the composite films with various thicknesses at different filler volume fractions.

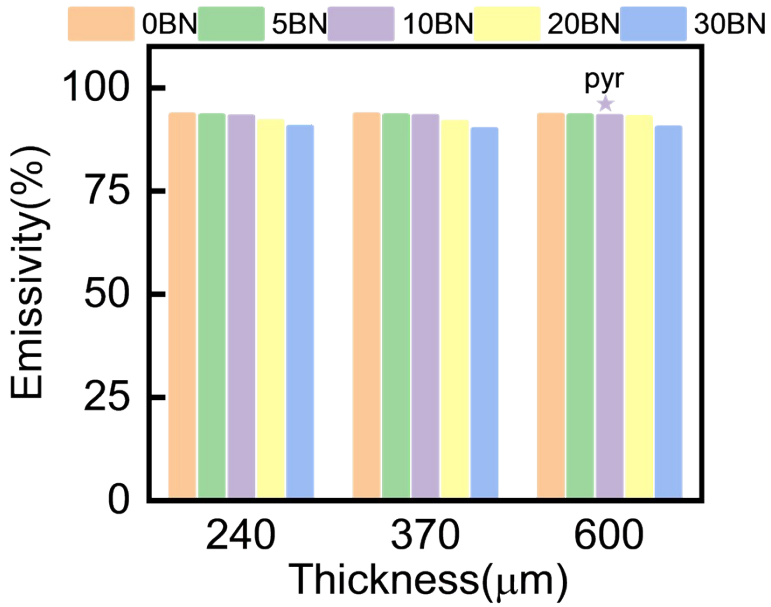

Fig. S14. Emissivity within the atmospheric transparency window of the composite films with various thicknesses at different filler volume fractions. The star symbol highlights the emissivity of the 600 μm-thick film featuring periodic pyramidal metastructure at a 10 vol% filler loading.

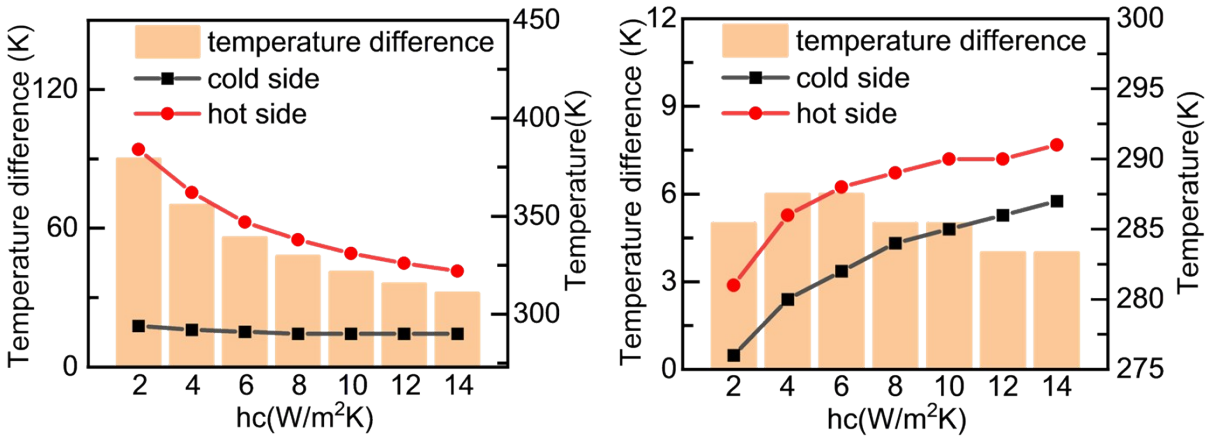

Fig. S15. Temperature difference (orange bars) and temperatures of the hot/cold sides (scatter points) under varying non-radiative heat transfer coefficients (hc) under solar irradiation (left) or dark (right) conditions.

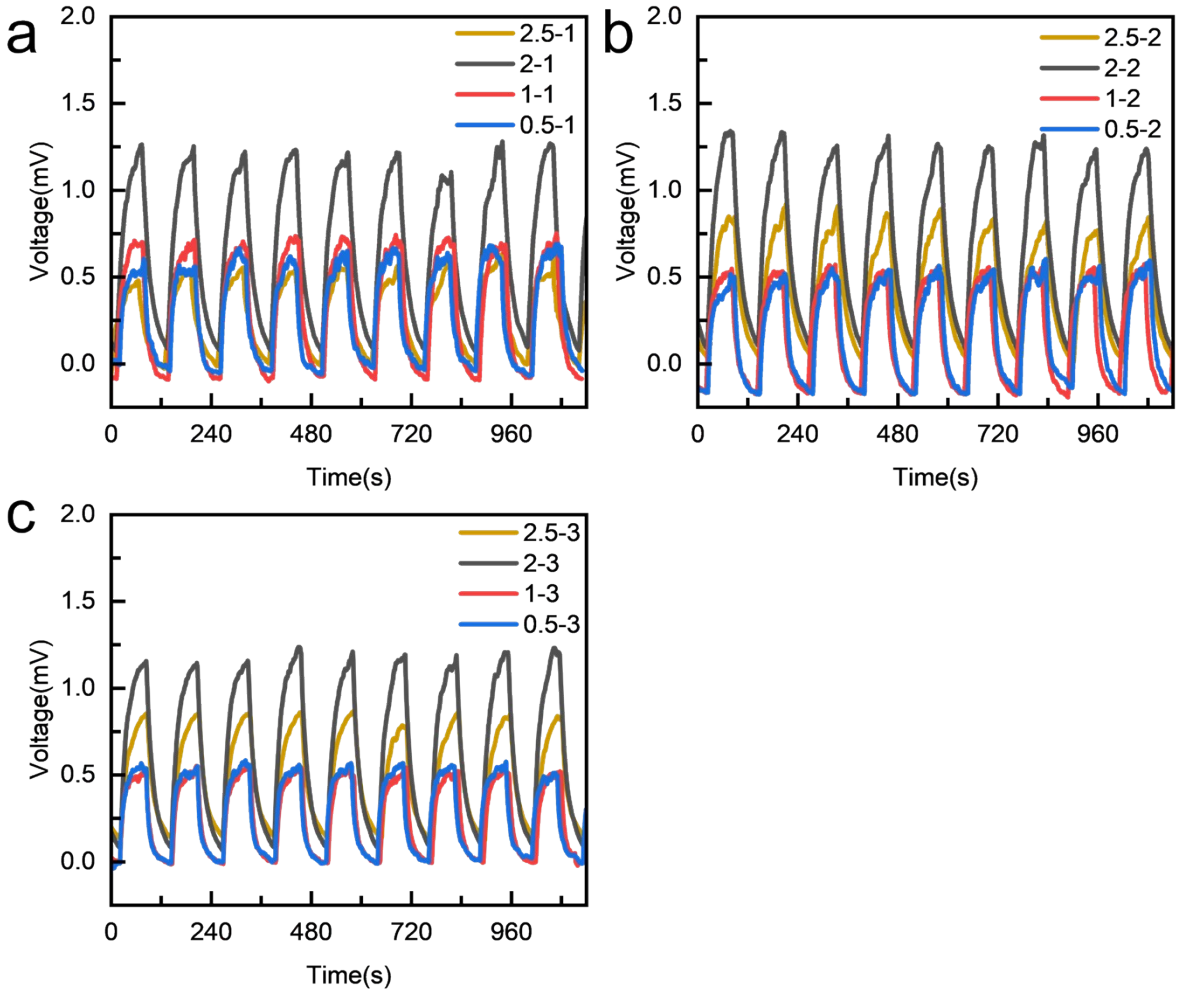

Fig. S16. Continuous output voltage of individual thermoelectric units with varying widths (0.5, 1.0, 2.0, and 2.5 cm) under a masked length of (a) 1 cm, (b) 2 cm, and (c) 3 cm.

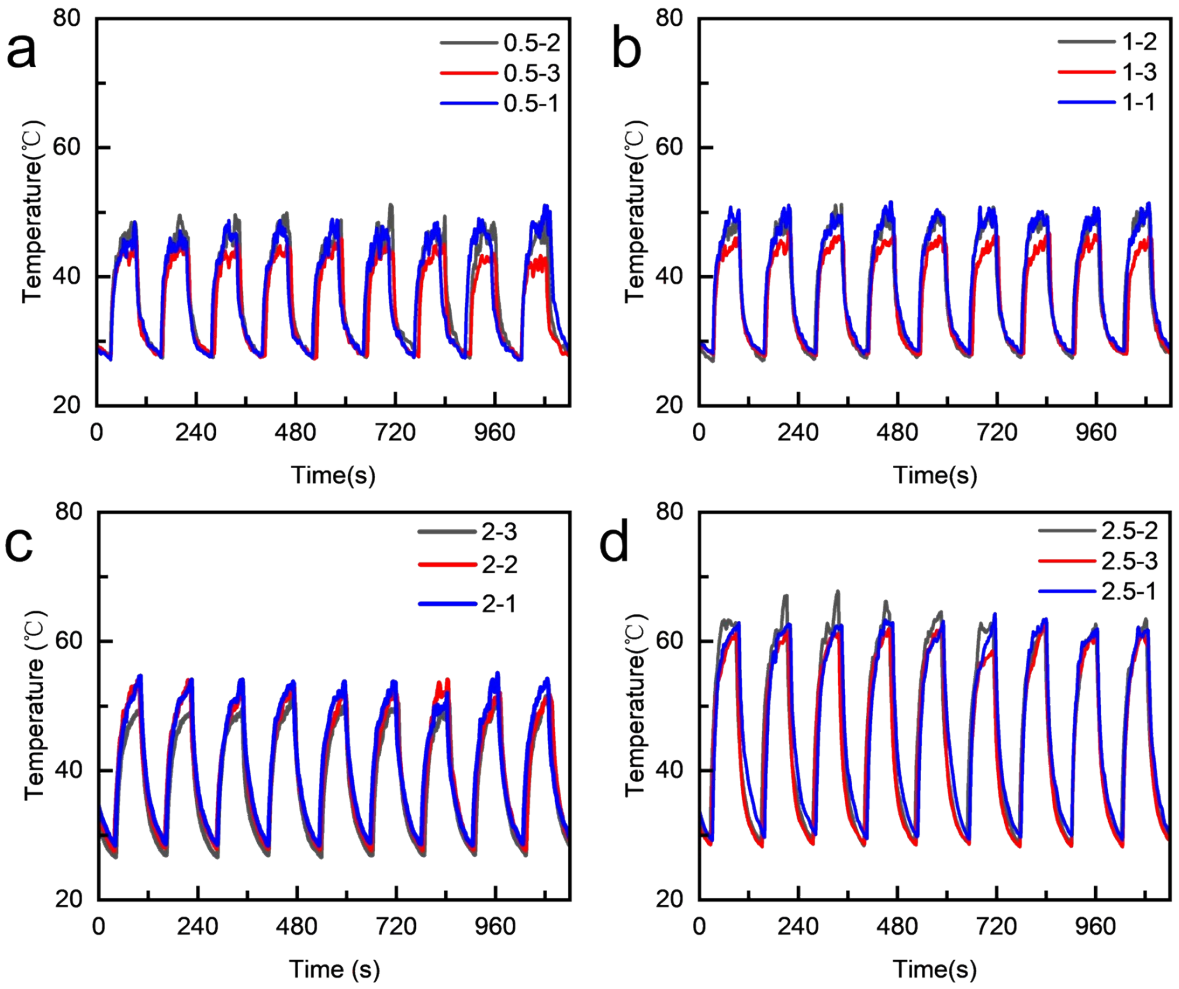

Fig. S17. Time-dependent temperature profiles at the hot end (a–d) for individual thermoelectric units with widths of (a) 0.5 cm, (b) 1.0 cm, (c) 2.0 cm, and (d) 2.5 cm.

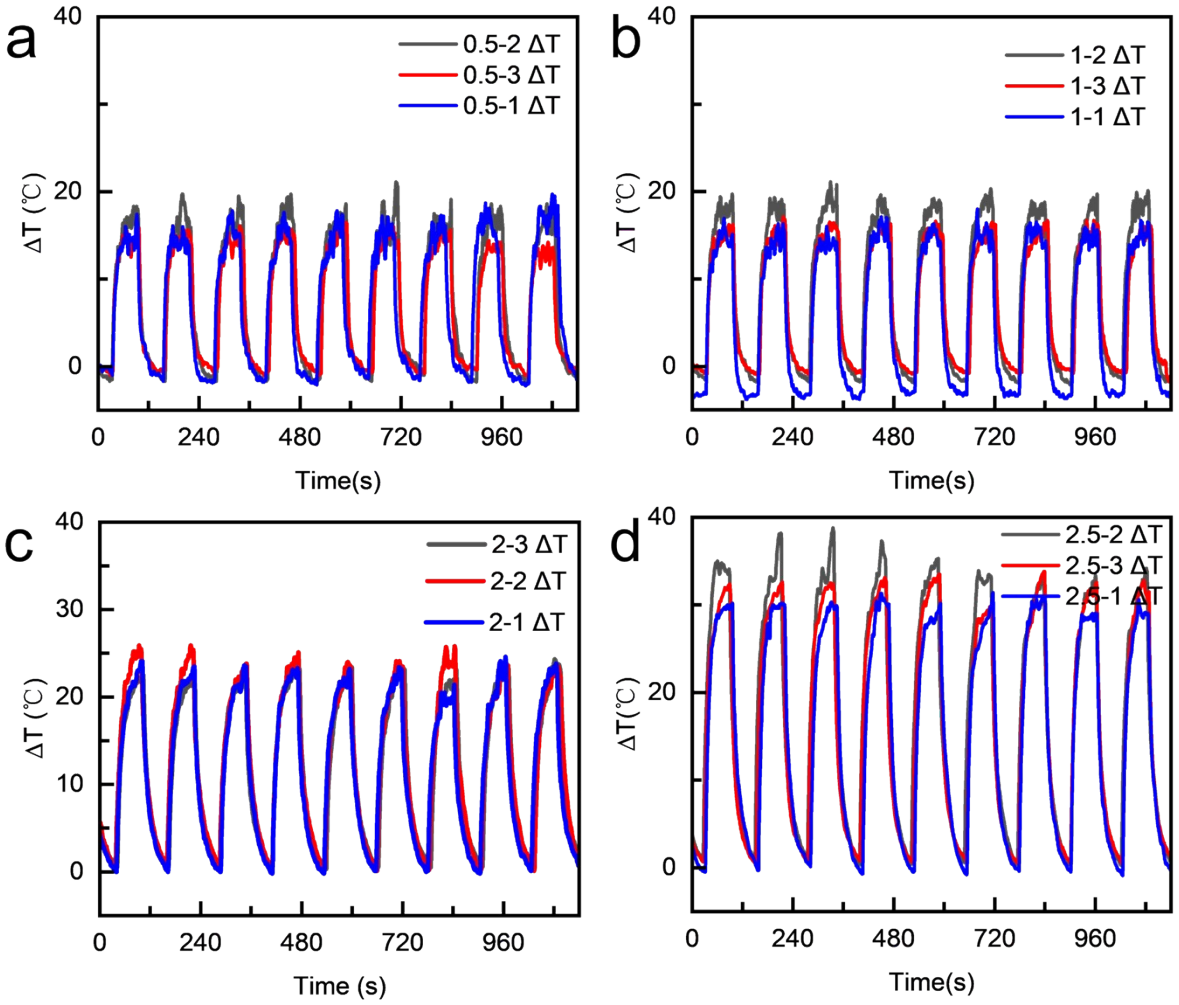

Fig. S18. Temperature differences between the cold and hot ends (a–d) for individual thermoelectric units with widths of (a) 0.5 cm, (b) 1.0 cm, (c) 2.0 cm, and (d) 2.5 cm.

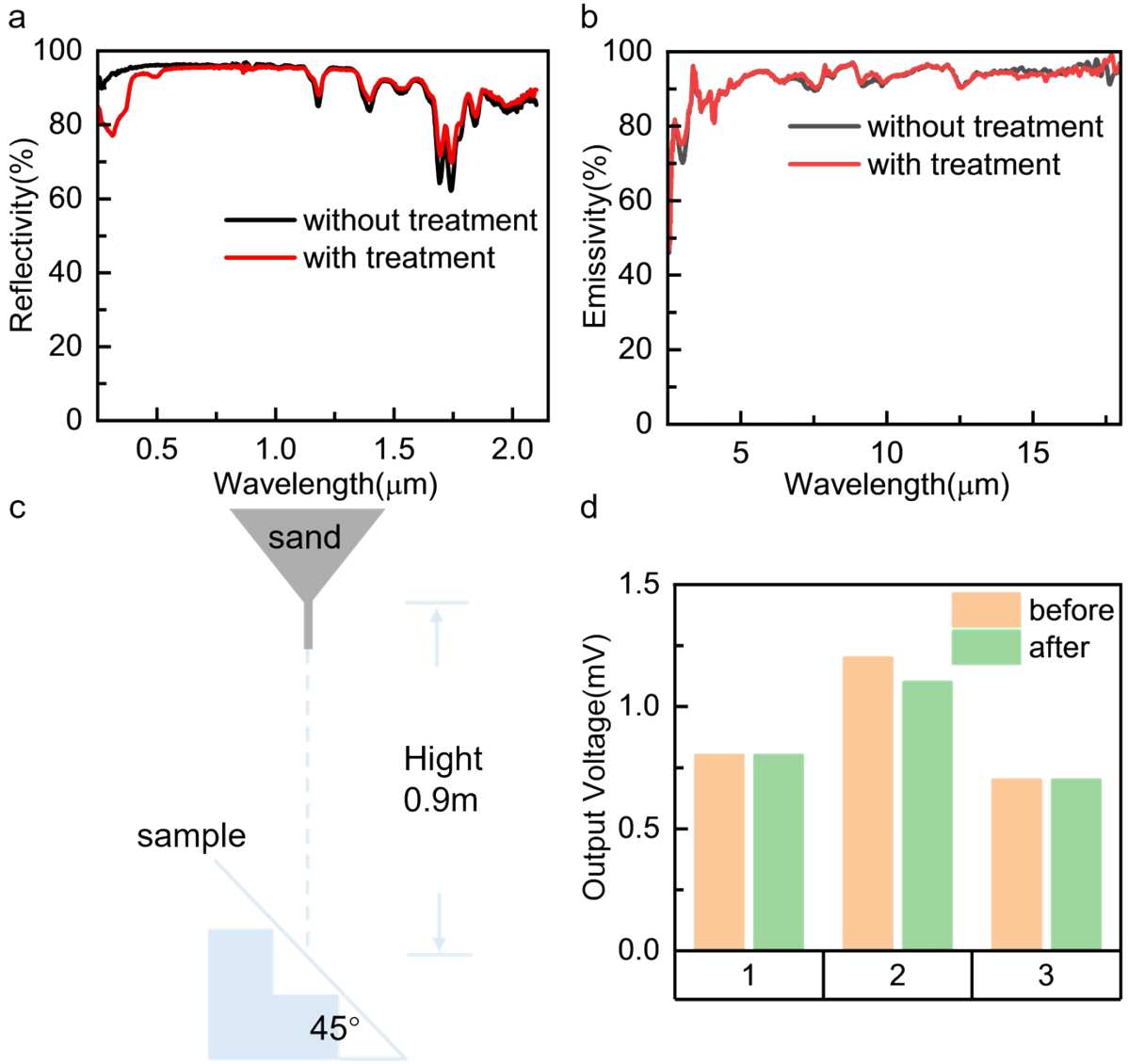

Fig. S19. Comprehensive durability tests of the device. (a) Spectral reflectance of the JPM before and after a sequential aging test (9 months of exposure in ambient humidity followed by a continuous 30-hour full-spectrum simulated solar irradiation at 1000 W/m^2). The overall solar reflectance exhibited a slight 2% decrease, with a localized minor drop observed in the UV band (~320 nm). (b) Mid-infrared emissivity spectra of the pyramid-structured film before and after the sand abrasion test. (c) Schematic illustration of the sand abrasion setup, where 2 kg of sand was continuously dropped from a height of 0.9 m onto the sample tilted at an angle of 45°. (d) Output voltages of three separate CNT samples measured under identical conditions before and after a 48-hour exposure to a high-humidity environment (85% relative humidity), demonstrating stable moisture tolerance.

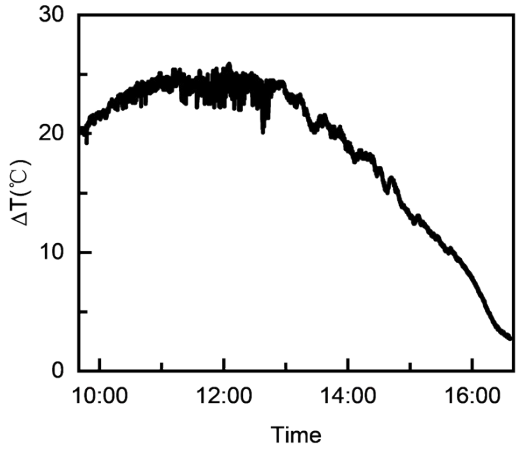

Fig. S20. Real-time temperature differential generated by the JPM-TED under natural solar irradiation on October 21, 2025.

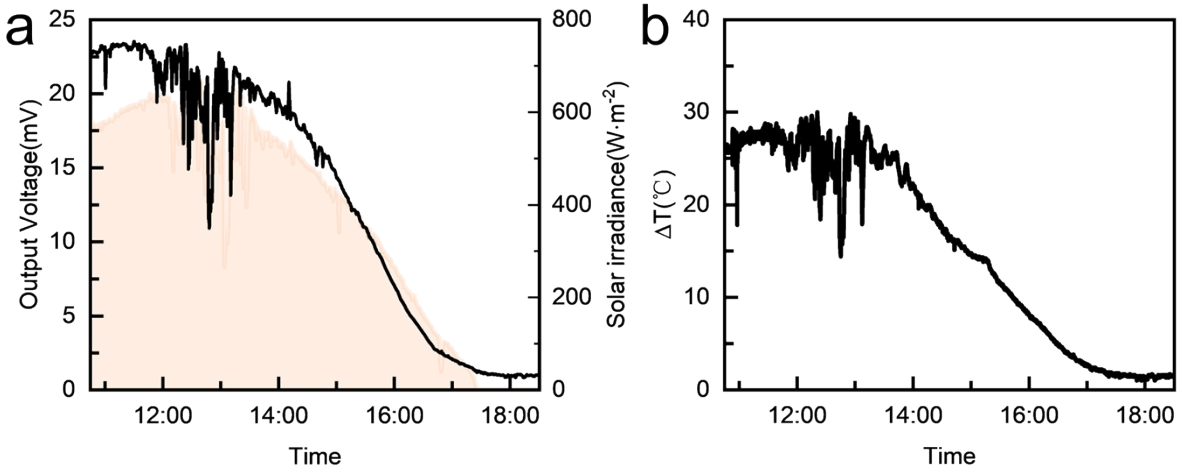

Fig. S21. (a) Output voltage and (b) temperature difference of the JPM-TED under solar radiation on October 20, 2025.

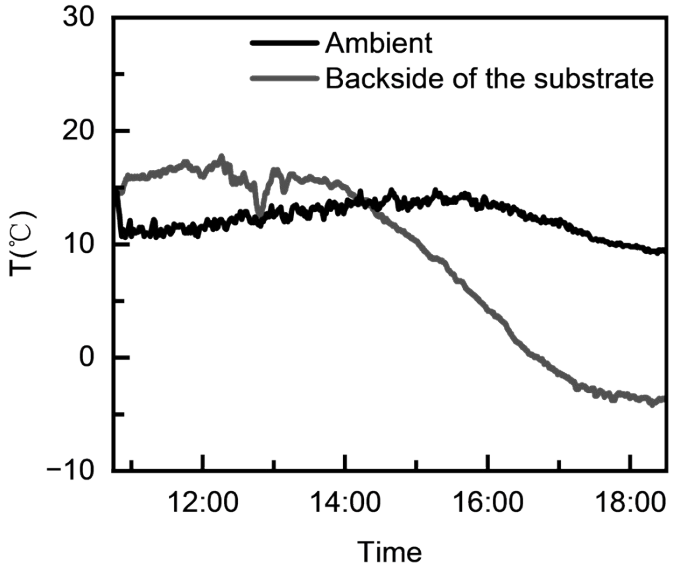

Fig. S22 Real-time monitoring of the JPM-TED back-surface temperature and the corresponding ambient temperature on October 20, 2025.

Table S1. Comprehensive comparison of state-of-the-art RC-TED systems.

Structure	Cold side	RC-TE connecting/ heat transfer mechanisms	Substrate	Limitations/ Advantages	References
origami-inspired structure	PVDF-HFP/Al_2O_3	adhesives/ indirect heat conduction	paper substrate	structurally unstable with paper, additional interfacial thermal resistance	[1]
freestanding PTE	silver films	Cover/ restricted heat conduction	without substrate	silver with low MIR emissivity; lacks a functional substrate, limiting practical viability	[2]
CNT–based thermoelectric arrays on conventional textile	PVDF-HFP nanofiber membranes	directly spun (gravity)/ restricted heat conduction	commercial white fabric	(RC-TE) loose interfacial bonding hinders cross-interface heat flux	[3]
Vertical stack	BN/PDMS	Coating/ restricted heat conduction	expanded graphite powder/ EGaIn/PDMS	inflicting undesirable thermal burden on skin	[4]
Rigid	P(VdF-	adhesives/	black chrome	bulky design; fails	[5]

assembly	HFP)/Al_2O_3 on Cu substrate	indirect heat conduction	film on Al substrate	to form conformal contact on curved surfaces	
wavy nanowire architecture	PDMS on commercial ESR substrate	cover/ restricted heat conduction	Te nanowires/TPU	susceptible to structural deformation; restricted interfacial contact area limits heat transfer	[6]
Monolithic sandwich structure	**Janus photonic metamaterial**	**Seamless interfacial contact for direct heat transfer**	**composite with high MIR emissivity**	**stable planar architecture; adhesive-free integration; protects underlying objects from downward heat accumulation**	**This work**

Table S2. Comparison of the output power performance among different thermoelectric devices.

Materials	Solar irradiance (W/m^2)	Temperature differences (K)	Maximum power density (mW/m^2)	References
PEDOT:PSShydrogel/ EMIM-TFSI/glycerol-90 hydrogel	/	24	15.5	[7]
CNTs	800	37	0.32	[3]
CNT/Bi_2Te_3	/	25	9.3	[8]
CNT	2000	/	3.2	[2]
CNTs	**600**	**24**	**12.27**	**This work**

Table S3. Comparison of the output voltage performance among different thermoelectric devices.

Materials	Solar irradiance (W/m^2)	Temperature differences (K)	Output voltage (mV)	References
PEI CNTs/ CNTs	550	/	12	[1]
PEI CNTs/PAA CNTs	1000	20	14	[9]
MXene/MWCNT/PEDOT:PSS	/	20	<0.8	[10]
PEDOT:PSShydrogel/EMIM-TFSI/glycerol-90 hydrogel	/	30	4.9	[7]
CNTs/ NDI	/	30	5.82	[11]
CNTs	**620**	**27.5**	**23.4**	**This work**

References

1. Q. Sun, C. Du, B. Huo, Z. Ding, W. Li and G. Chen, Advanced Functional Materials, 2025, n/a, e18493.
2. X. Dai, Y. Wang, X. Sun, K. Li, J. Pan, J. Wang, T. Zhuang, D. Chong, J. Yan and H. Wang, Advanced Materials, 2024, 36, 2312570.
3. J.-Z. Liu, W. Jiang, S. Zhuo, Y. Rong, Y.-Y. Li, H. Lu, J. Hu, X.-Q. Wang, W. Chen, L.-S. Liao, M.-P. Zhuo and K.-Q. Zhang, Science Advances, 2025, 11, eadr2158.
4. S. Zhu, L. Miao, J. Gao, J.-l. Chen, Q. Zhou, Z. Pan, Z. Zhang, J. Liang, X. Yang and T. Mori, Nano Energy, 2025, 144, 111328.
5. K. Liu, Y. Ma, Y. Li, Y. Wu, C. Fu and T. Zhu, Advanced Science, 2024, 11, 2309871.
6. C. Chen, R. Wang, X.-L. Li, B. Zhao, H. Wang, Z. Zhou, J. Zhu and J.-W. Liu, Nano Letters, 2022, 22, 4131–4136.
7. J. Wang, Q. Li, K. Li, X. Sun, Y. Wang, T. Zhuang, J. Yan and H. Wang, Advanced Materials, 2022, 34, 2109904.
8. Y. Li, J. Qiao, Y. Zhao, Q. Lan, P. Mao, J. Qiu, K. Tai, C. Liu and H. Cheng, Journal of Materials Science & Technology, 2020, 58, 80–85.
9. H. Wang, Q.-R. Yang, X.-F. Feng, X.-L. Li and J.-W. Liu, ACS Nano, 2025, 19, 39925–39935.
10. C. Zhang, P.-a. Zong, Z. Ge, Y. Ge, J. Zhang, Y. Rao, Z. Liu and W. Huang, Nano Energy, 2023, 118, 109037.
11. R. Niu, C. Pan, Z. Chen, L. Wang and L. Wang, Chemical Engineering Journal, 2020, 381, 122650.